

This is a repository copy of *Traceable characterisation of fibre-coupled single-photon detectors*.

White Rose Research Online URL for this paper:

<https://eprints.whiterose.ac.uk/217592/>

Version: Published Version

Article:

Arabskyj, Luke, Dolan, Philip R., Parke, Adam L. et al. (6 more authors) (2024) Traceable characterisation of fibre-coupled single-photon detectors. *Metrologia*. 055008. ISSN 1681-7575

<https://doi.org/10.1088/1681-7575/ad70bc>

Reuse

This article is distributed under the terms of the Creative Commons Attribution (CC BY) licence. This licence allows you to distribute, remix, tweak, and build upon the work, even commercially, as long as you credit the authors for the original work. More information and the full terms of the licence here:

<https://creativecommons.org/licenses/>

Takedown

If you consider content in White Rose Research Online to be in breach of UK law, please notify us by emailing eprints@whiterose.ac.uk including the URL of the record and the reason for the withdrawal request.



PAPER • OPEN ACCESS

Traceable characterisation of fibre-coupled single-photon detectors

To cite this article: Luke Arabskyj *et al* 2024 *Metrologia* **61** 055008

View the [article online](#) for updates and enhancements.

You may also like

- [A new interpolation equation in the ITS-90 subrange from the triple point of water to the freezing point of indium](#)
Kang Lan, Lide Fang, Ying Wang et al.
- [Trap induced broadening in a potential hydrogen lattice clock](#)
J P Scott, R M Potvliege, D Carty et al.
- [Quantum plasmonic sensing by Hong–Ou–Mandel interferometry](#)
Seungjin Yoon, Yu Sung Choi, Mark Tame et al.

Traceable characterisation of fibre-coupled single-photon detectors

Luke Arabsky^{1,2,*} , Philip R Dolan¹ , Adam L Parke¹, Ted S Santana¹ , Simon R G Hall¹ , Geiland Porrovecchio³, Marek Smid³, Marco Lucamarini²  and Christopher J Chunnillall¹ 

¹ National Physical Laboratory, Hampton Road, Teddington TW11 0LW, United Kingdom

² School of Physics, Engineering & Technology and York Centre for Quantum Technologies, Institute for Safe Autonomy, University of York, York YO10 5FT, United Kingdom

³ Český Metrologický Institut (CMI), Okružní 31, 63800 Brno, Czech Republic

E-mail: luke.arabsky@npl.co.uk and la1225@york.ac.uk

Received 27 March 2024, revised 12 July 2024

Accepted for publication 19 August 2024

Published 9 September 2024



CrossMark

Abstract

The detection of single photons plays an essential role in advancing single-photon science and technologies. Yet, within the visible/near-infrared spectral region, accurate fibre-based optical power measurements at the few-photon level are not yet well-established. In this study, we report on a fibre-based setup, enabling traceable optical power measurements at the few-photon level in this spectral region. The setup was used to calibrate the detection efficiency (DE) of four single-photon avalanche diode (SPAD) detectors. The relative standard uncertainties on the mean DE values obtained from repeat fibre-to-detector couplings ranged from 0.67% to 0.81% ($k = 2$). However, the relative standard deviation of DE values, which ranged from 1.38% to 3.20% ($k = 2$), poses a challenge for the metrology of these devices and applications that require high accuracy and repeatability. We investigated the source of these variations by spatially mapping the response of a detector's fibre connector port, using a focused free-space beam, allowing us to estimate the detector's spatial non-uniformity. In addition, we realise a novel calibration approach for fibre-coupled SPADs in a free-space configuration, enabling a direct comparison between the fibre-based setup and the National Physical Laboratory's established free-space facility using a single SPAD. Finally, we investigated alternative coupling methods, testing the repeatability of different fibre-to-fibre connectors in addition to direct fibre-to-detector couplings: SPADs from three manufacturers were tested, with both single-mode and multi-mode fibre.

Keywords: single-photon avalanche diode, Si-SPAD, fibre-coupled, detection efficiency, detector calibration, repeatability, SI traceable

1. Introduction

Single-photon detectors are being used in an expanding range of applications—see figure 1 in [1]. Examples include

low-light sensing and surveillance [2], medical imaging [3, 4] and astronomy [5, 6]. Another category of applications covers new and emerging quantum technologies, such as quantum random number generation [1, 7] and quantum key distribution (QKD) [8–14].

The performance of these applications, along with many others, are highly dependent on the parameters of the single-photon detectors employed, driving a corresponding need for enhanced metrological measurement capabilities. As a result, many national metrology institutes (NMIs) have committed significant efforts to the development of SI traceable

* Author to whom any correspondence should be addressed.



Original Content from this work may be used under the terms of the [Creative Commons Attribution 4.0 licence](https://creativecommons.org/licenses/by/4.0/). Any further distribution of this work must maintain attribution to the author(s) and the title of the work, journal citation and DOI.

optical power measurements at the few-photon level. Across the visible/near-infrared (vis/NIR) region of the spectrum there are well-established capabilities in free-space [15–23] and similar across the telecom C-band in fibre [15, 24–28]. However, fibre-based capabilities in the vis/NIR are less well-established, as are those in free-space within the telecom C-band [29]. With some applications now traversing the interface between these two optical channels [30, 31], efforts must now be made to fill these gaps.

In this work we present a simple, easy-to-assemble set-up which addresses the need for SI traceable optical power measurements in fibre in the vis/NIR spectral region. This set-up was used to measure the detection efficiency (DE) of four low-noise Hamamatsu C13001-01 single-photon avalanche diodes (SPADs), labelled SN1 through SN4. Measurements were traceable to the National Physical Laboratory’s (NPL’s) primary optical standard [32] at a wavelength of 633 nm. In addition, for the first time, we demonstrate the calibration of a fibre-coupled device in a free-space setup, enabling a direct comparison between these two optical configurations on a single SPAD. We then use this technique to compare the DE results obtained from the fibre setup with those from NPL’s established free-space detector calibration facility [23, 33]. Finally, we present the results of an investigation into alternative fibre-to-detector coupling methods in an effort to improve the measurement repeatability of future measurements. This work is an important step towards establishing a suite of metrological measurement capabilities, spanning both spectral bands, within fibre and free-space channels.

2. Measurement setup and characterisation

The experimental approach comprises two steps: firstly, the attenuation between a monitor photodiode and a calibrated reference photodiode is measured; secondly, this attenuation factor is applied to a series of low-power measurements with a single-photon detector in place of the reference detector. The focus of this section is on the first step.

Figure 1 illustrates the setup. The photon source is a continuous wave (CW) 633 nm pigtailed laser diode which is coupled to two variable optical attenuators (VOAs) in series by single-mode fibre (SMF): VOA (1) limits the optical power and VOA (2) is used to vary the power to a desired photon flux over a 40 dB range. The second VOA is connected to an Agiltron 1×2 optical micro-electro-mechanical system (MEMS) switch with a crosstalk extinction greater than 60 dB that serves as a fibre shutter. For background measurements, light is terminated into a Thorlabs FTAPC1 fibre-optic terminator; for light measurements the optical path is switched, and the light is split into two channels via a 99:1 fibre-splitter: the 99% arm is the monitor channel, and the 1% arm is the start of the attenuated channel. The monitor channel is connected to a photodiode (PD_{mon}) and the corresponding photocurrent (I_{mon}) is amplified and converted into a voltage (V_{mon}) by a calibrated trans-impedance amplifier (TIA). The TIA is connected to a calibrated digital voltmeter (DVM) which is read by automated LabVIEW software. The attenuated channel begins

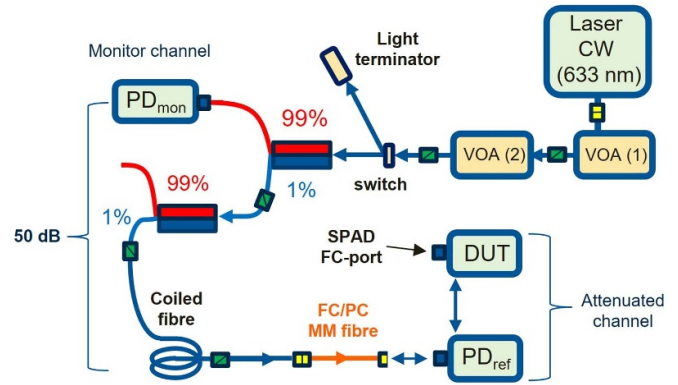


Figure 1. Schematic of the experimental setup. A continuous wave (CW) 633 nm pigtailed laser diode is connected to either the device under test (DUT) or the reference photodiode (PD_{ref}) via two variable optical attenuators (VOAs), an optical MEMS switch, two 99:1 fibre-beam-splitters, a coiled fibre and a multi-mode (MM) fibre. The laser power is monitored with photodiode PD_{mon} . Green rectangles mark ferrule connector/angled physical contact (FC/APC) connections and yellow rectangles mark ferrule connector/physical contact (FC/PC) connections.

with the output of the 1% arm of the first fibre-splitter which is connected to a second 99:1 fibre-splitter. A coiled fibre, with a coil diameter of 25 mm, is linked to the 1% output of this second splitter, serving to remove cladding modes. The final fibre of the attenuation channel is a multi-mode fibre (MMF) with a 50 μm core diameter. The total attenuation of the channel, which is of the order of 50 dB, is due to the fibre-splitters and the combined insertion loss of the fibre connections. The output of the MMF, which is used in this study as it matched the fibre intended for use in the detectors’ application post-calibration, may be switched between a fibre-coupled reference photodiode (PD_{ref}) and a device under test (DUT). PD_{ref} is a windowless Hamamatsu S1337-1010BQ photodiode [34], calibrated in free-space with traceability to NPL’s cryogenic radiometer. Its output photocurrent I_{ref} is amplified and converted to a voltage (V_{ref}) by a calibrated switched integrator amplifier (SIA) [35, 36]. All fibre connections are ferrule connector/angled physical contact (FC/APC) with the exceptions being those to the MMF and the pigtail of the laser diode which are ferrule connector/physical contact (FC/PC); fibre suitable for single-mode propagation at 633 nm is used throughout, except for the MMF patch cord.

The attenuation factor (β) between the monitor channel and the attenuated channel is defined as the photocurrent ratio:

$$\beta = \frac{I_{\text{ref}}}{I_{\text{mon}}} = \frac{V_{\text{ref}}}{G_{\text{ref}}} \cdot \frac{G_{\text{mon}}}{V_{\text{mon}}}, \quad (1)$$

where G_{mon} and G_{ref} are the respective TIA and SIA amplifier gain coefficients. The optical powers must be above the noise floor of the reference diode which is in the order of picowatts; whilst the optical power incident upon the monitor diode must be less than 0.4 mW to ensure linearity [37]. As the fixed attenuation between the two channels is of the order of 50 dB, this gives approximately two orders-of-magnitude of optical power to perform the measurement. Although the

fixed attenuation could be reduced to increase this range, it would also reduce the signal-to-background (S/B) ratio of the monitor photodiode during the DE measurement. Finally, we note that the splitting ratios of the fibre-beam-splitters are temperature and polarisation dependent. We mitigated this effect by securely fixing all fibres to an optical table which provides mechanical stability and acts as a large heatsink within a 21.0(5) °C temperature stabilised lab. The temporal stability of the attenuation ratio (β) demonstrated the effectiveness of this approach, with a calculated relative standard deviation of approximately 0.1% over the 1.5 h measurement duration. A summary of the attenuation factor results can be found in appendix A.

3. Fibre-coupled detection efficiency

The optical power measured by the under-filled reference photodiode (P_{ref}) is equivalent to that exiting the MMF (P_{MM}) since there are no additional interfaces between the fibre and the photodiode's surface. Therefore, $P_{\text{ref}} = V_{\text{ref}} / (G_{\text{ref}} \cdot R_{633}) = P_{\text{MM}}$, where R_{633} is the spectral responsivity of PD_{ref} . The same applies when coupling to the FC-port of the SPAD. Within the FC-port, there is a fixed gradient-index (GRIN) lens which focuses the diverging beam onto the active area; however, this is considered as part of the detection system. By substituting the above equation into equation (1) and rearranging for P_{MM} the optical power can be inferred from the output voltage produced by PD_{mon} with

$$P_{\text{MM}} = \frac{V_{\text{mon}}}{G_{\text{mon}}} \cdot \frac{\beta}{R_{633}}. \quad (2)$$

It then follows that the mean number of photons exiting the MMF can be written as

$$N_{\text{inf}} = \frac{V_{\text{mon}}}{G_{\text{mon}}} \cdot \frac{\beta}{R_{633}} \cdot \frac{\lambda_{633}}{h \cdot c} \cdot C_{\text{div}}, \quad (3)$$

where N_{inf} is the inferred mean photon number per second, λ_{633} is the wavelength of the laser, h is Planck's constant, c is the speed of light and C_{div} is a correction factor which accounts for beam divergence as it exits the fibre (see section 5.4.3 for further information). With this, PD_{ref} may be switched for the DUT, and the input power reduced to an amount measurable by both the DUT and PD_{mon} . The DE (η) is then calculated as

$$\eta = \frac{N_{\text{counts}} - N_{\text{bg}}}{N_{\text{inf}} (1 - N_{\text{counts}} \cdot \tau_{\text{d}})}, \quad (4)$$

where N_{counts} is the averaged number of recorded detection events per second, N_{bg} is the averaged number of recorded background counts per second and τ_{d} is the detector's dead time which is measured in a separate experiment (see section 5.6). $(N_{\text{counts}} - N_{\text{bg}}) / (N_{\text{inf}})$ is defined as the detection probability which appears to decrease as a function of incident photon number. This decrease is primarily due to detector dead time [38]: as the detector spends an increasing proportion of the time in its off-state the number of missed photons also

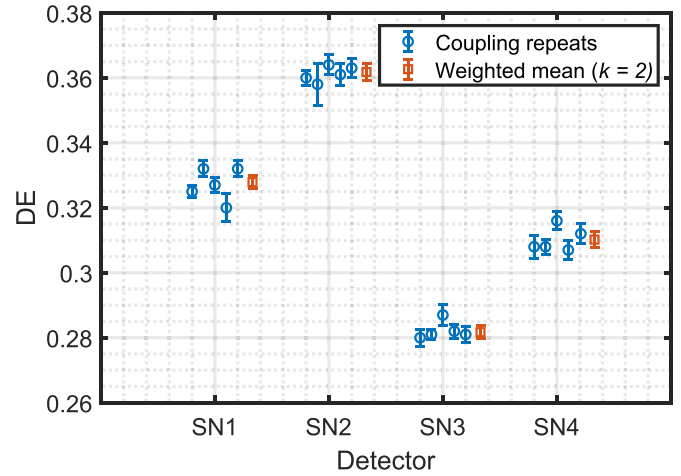


Figure 2. Photon detection efficiencies for the Hamamatsu detectors.

increases, the $(1 - N_{\text{counts}} \tau_{\text{d}})^{-1}$ factor corrects for this and is commonly applied to devices with a fixed dead time [39]. A short derivation of equation (4) which also considers the source statistics is presented in appendix B. In all measurements the number of incident photons upon the detector was set to approximately 10^5 per second by VOA 2. The detector S/B ratios were greater than 10^3 , with the average background counts registered by each detector being less than 5 per second. However, at these optical powers the monitor S/B ratios were as low as 1.6.

4. Measurement results

Five measurements for each detector were performed, each measurement contained a series of five light and dark exposures. Each light exposure was followed by a dark exposure. Light exposures were taken for five seconds, with twenty-five readings measured for 0.2 s each. However, due to a latency between readings in our software, the twenty-five light readings are recorded over approximately 13 s. This duration is close to the optimum integration time of around 30 s as subsequently determined from the Allan deviation of the laser's optical power. Dark exposures were constructed from ten readings, each measured for 0.2 s. The number of dark readings was reduced due to the negligible background count rates; for detectors with higher intrinsic dark count rates and/or increased background levels, longer exposures are required. Between each measurement, the MMF was disconnected from the SPAD's FC-port, cleaned, inspected, and reconnected to test the coupling repeatability. Figure 2 displays the measurement results. Blue circles mark the five fibre-to-detector coupling repeats, with error bars marking standard uncertainties. Orange squares mark the weighted mean of the five coupling repeats for each detector, with an overall expanded uncertainty at $k = 2$.

The origin of the larger error bars for a specific coupling, which are most prominent in SN1 and SN2, have been traced to fluctuations in the monitor photodiode's output voltage (V_{mon}).

Table 1. Summary of detection efficiency results obtained from repeat couplings, including standard uncertainties (Std. Unc.) and standard deviations (Std. Dev.).

| Detector | Detection efficiency $\bar{\eta}_d$ | Std. Unc. $U(\bar{\eta}_d)$ ($k = 2$) | Std. Dev. ($k = 2$) |
|----------|-------------------------------------|---|-----------------------|
| SN1 | 0.3279 | 0.0022 | 0.0105 |
| SN2 | 0.3618 | 0.0027 | 0.0050 |
| SN3 | 0.2817 | 0.0020 | 0.0052 |
| SN4 | 0.3102 | 0.0025 | 0.0072 |

These fluctuations were not evident in the count rate recorded simultaneously by the SPAD detector, indicating they are not optical in origin. Although the exact cause is uncertain at present, they may be due to thermoelectric potentials at the μV level which could be reduced by increasing the amplification gain. They may also be statistical, arising from operating the monitor close to its noise floor.

The results are summarised in table 1. The weighted mean and its associated standard uncertainty (Std. Unc.) provide the best estimate of the detector's efficiency, as they are based on multiple repeat fibre couplings. The standard deviation (Std. Dev.) of repeat couplings is also significant and are therefore included in the table; a single coupling of the detector should take into account this $k = 2$ value, which provides a 95% confidence that the DE will fall within the uncertainty obtained by combining the Std. Unc. and the Std. Dev. in quadrature. Both these uncertainties should be provided as part of a calibration.

The weighted mean DE value for each detector $\bar{\eta}_d$ was calculated with

$$\bar{\eta}_d = \frac{\sum_{i=1}^n w_i \cdot \eta_{d,i}}{\sum_{i=1}^n w_i}, \quad (5)$$

where η_i and w_i are the respective efficiency and weighting of the i th coupling measurement; w_i is defined by the i th coupling's standard uncertainty $U(\eta_{d,i})$:

$$w_i = U(\eta_{d,i})^{-2}.$$

The combined standard uncertainty of the mean value is then

$$U(\bar{\eta}_d) = \frac{1}{\sqrt{\sum_{i=1}^n U(\eta_{d,i})^{-2}}}, \quad (6)$$

where n is the number of repeat couplings. $U(\bar{\eta}_d)$ is then expanded to the 95% confidence interval with a coverage factor k obtained from Student's t-inverse function with the measurement's effective degrees of freedom, as described in sections G.4.1 and C.3.8 of the Guide to the Expression of Uncertainty in Measurement (GUM) [40].

5. Measurement uncertainty

Table 2 summarises the measurement uncertainty for the DE of detector SN1. It comprises three distinct components/sections. The first (uppermost) section covers the attenuation factor measurement (β -equation (1)) at a single optical power

following the measurement procedure outlined in section 2. The second section covers the calculation of the inferred mean photon number (N_{inf} -equation (3)) for a single coupling measurement at a constant photon flux, as described in section 3. The attenuation factor used in this calculation is an average of repeated measurements across multiple optical powers and is therefore denoted by $\bar{\beta}$. The third section covers the calculation of the detector's DE obtained from the first coupling ($\eta_{\text{SN1,1}}$ -equation (4)). Below this, within the fourth section, is $\bar{\eta}_{\text{SN1}}$ —the weighted mean value which was presented in table 1. The total expanded uncertainty was calculated with a coverage factor of $k = 2.02$ with $\nu = 43$ effective degrees of freedom. In the following subsections each component is considered in detail.

5.1. Constants

Planck's constant: $h = 6.62607015 \cdot 10^{-34}$ Js.

Speed of light in vacuum: $c = 299\,792\,458$ ms $^{-1}$.

5.2. Wavelength

The optical spectrum of the Thorlabs pigtailed laser diode (LP633-SF50) was measured with a Yokogawa AQ6370D optical spectrum analyser (OSA) which was calibrated to the vacuum wavelength transition of the HeNe line at approximately 633 nm. A conservative uncertainty was given, which is obtained from the full width at half maximum (FWHM) of the spectral power distribution

$$\lambda_{633} = 632.97 \pm 0.49 \text{ nm.}$$

5.3. Spectral responsivity

The spectral responsivity of the reference photodiode was calibrated in free-space against a reference 3-element-trap detector, whose calibration is traceably linked to NPL's cryogenic radiometer, the primary standard for optical power [32]. The calibration was performed with the same laser used throughout this study in NPL's free-space calibration facility [23, 33]

$$R_{633} = 0.35260(57) \text{ AW}^{-1}.$$

5.4. Voltages and amplification gain coefficients

Calibrated amplifiers were used to convert the monitor and reference photodiode output currents to measurable voltages. Voltages were read with calibrated Keithley 2000 DVMs. Calibrations were performed internally at NPL^{4,5}.

5.4.1. Reference photodiode. The reference photodiode was used in the characterisation of the attenuation factor (β).

⁴ National Physical Laboratory, Department of Electromagnetic & Electrochemical Technologies, London, TW11 0LW.

⁵ National Physical Laboratory, Department of Optical Radiometry, London, TW11 0LW.

Table 2. Uncertainty budget for a single detection efficiency measurement performed on detector SN1. The combined standard uncertainties were calculated as described in section 5 of the Guide to the Expression of Uncertainty in Measurement [40], see section 5.1.3 for information on sensitivity coefficients and contributions. The presented values are truncated for clarity; however, all calculations were performed using the full precision of the data. Uncertainties are presented at $k = 1$ unless stated otherwise.

| Measurand | Value | Standard uncertainty (u) | Distribution | Sensitivity coefficient (c) | Contribution ($u \cdot c$) | Relative contribution ($u \cdot c$) ² / U^2 |
|---------------------------|--------------------------------------|---|--------------|---|---------------------------------|---|
| V_{mon} | 3.1025 V | $7.5218 \cdot 10^{-4}$ V | Normal | $-1.1409 \cdot 10^{-5}$ V ⁻¹ | $-8.5824 \cdot 10^{-9}$ | 0.3383 |
| G_{mon} | $9.9985 \cdot 10^3$ VA ⁻¹ | 0.9998 VA ⁻¹ | Normal | $3.5404 \cdot 10^{-9}$ AV ⁻¹ | $3.5399 \cdot 10^{-9}$ | 0.0575 |
| V_{ref} | 10.9945 V | $3.156 \cdot 10^{-3}$ V | Normal | $3.2197 \cdot 10^{-6}$ V ⁻¹ | $1.0164 \cdot 10^{-8}$ | 0.4745 |
| G_{ref} | $1.0009 \cdot 10^9$ VA ⁻¹ | $1.5014 \cdot 10^5$ VA ⁻¹ | Normal | $-3.5366 \cdot 10^{-14}$ AV ⁻¹ | $-5.3099 \cdot 10^{-9}$ | 0.1295 |
| β | $3.5400 \cdot 10^{-5}$ | $1.4754 \cdot 10^{-8}$ | Normal | | | |
| h | $6.62607015 \cdot 10^{-34}$ Js | | | | 0 | 0 |
| c | 299 792 458 ms ⁻¹ | | | | 0 | 0 |
| λ | 632.97 nm | 0.4900 nm | Normal | $1.4161 \cdot 10^{11}$ m ⁻¹ s ⁻¹ | 69.3891 s ⁻¹ | 0.0117 |
| $\bar{\beta}$ | $3.5341 \cdot 10^{-5}$ | $4.6312 \cdot 10^{-9}$ | Normal | $2.5363 \cdot 10^9$ s ⁻¹ | 11.7461 s ⁻¹ | 0.0003 |
| V_{mon} | $2.8056 \cdot 10^{-5}$ V | $1.3348 \cdot 10^{-7}$ V | Normal | $3.1949 \cdot 10^9$ V ⁻¹ s ⁻¹ | 426.4540 s ⁻¹ | 0.4448 |
| G_{mon} | $9.9964 \cdot 10^4$ VA ⁻¹ | 9.9964 VA ⁻¹ | Normal | $8.9667 \cdot 10^{-1}$ AV ⁻¹ s ⁻¹ | 8.9635 s ⁻¹ | 0.0002 |
| R_{633} | 0.3526 AW ⁻¹ | $5.7122 \cdot 10^{-4}$ AW ⁻¹ | Normal | $2.5421 \cdot 10^5$ WA ⁻¹ s ⁻¹ | 145.21 s ⁻¹ | 0.0516 |
| C_{div} | 1.000 | 0.005 | Rectangular | $8.9635 \cdot 10^4$ s ⁻¹ | 448.1755 s ⁻¹ | 0.4910 |
| N_{inf} | 89 635 s ⁻¹ | 639.4088 s ⁻¹ | Normal | | | |
| N_{counts} | 29 744 s ⁻¹ | 46 s ⁻¹ | Poissonian | $1.1172 \cdot 10^{-5}$ s | $5.0887 \cdot 10^{-4}$ | 0.0441 |
| N_{inf} | 89 635 s ⁻¹ | 639 s ⁻¹ | Normal | $-3.7046 \cdot 10^{-6}$ s | $-2.3688 \cdot 10^{-3}$ | 0.9558 |
| τ_{d} | $23.2 \cdot 10^{-9}$ s | $5 \cdot 10^{-10}$ s | Normal | $9.8839 \cdot 10^3$ s ⁻¹ | $4.9419 \cdot 10^{-6}$ | 0.0000 |
| $\eta_{\text{SN1},1}$ | 0.3320 | 0.0024 | Normal | | | |
| $\bar{\eta}_{\text{SN1}}$ | 0.3279 | 0.0022 ($k = 2$) | Normal | | | |

To ensure linearity, β is measured over a range of powers as described in section 2; the voltage presented below corresponds to a single optical power.

Gain coefficient: $G_{\text{ref}} = 1.00090(15) \cdot 10^9$ VA⁻¹; Mean voltage: $V_{\text{ref}} = 10.9946(32)$ V.

5.4.2. Monitor photodiode. The monitor photodiode is required for measuring the attenuation factor (β) and inferring the mean photon number (N_{inf}). In both these measurements the uncertainty in the voltage output of the TIA is significant and may be attributed to the inherent noise characteristics associated with low-level optical powers. The voltages presented below correspond to single optical powers.

β measurement, gain coefficient: $G_{\text{mon}} = 9.9985(10) \cdot 10^3$ VA⁻¹; mean voltage: $V_{\text{mon}} = 3.1025(8)$ V.

N_{inf} measurement, gain coefficient: $9.9964(10) \cdot 10^4$ VA⁻¹; mean voltage: $V_{\text{mon}} = 2.806(13) \cdot 10^{-5}$ V.

5.4.3. Beam divergence correction. As the spectral responsivity of the reference photodiode was calibrated with a collimated beam, an additional uncertainty factor is included to account for the beam divergence as it exits the fibre during the characterisation of β . This dominant uncertainty contribution, which is dependent on the purity of the polarisation, is not expected to be significant from the Fresnel equations. However, by measuring the photodiode's response with a collimated beam as a function of incidence angle, a dependence was determined empirically. The maximum variation of the photodiode's response with respect to incident angle was

then used as the uncertainty contribution. We anticipate that this conservative estimate may be reduced with further work

$$C_{\text{div}} = 1.000(5) \text{ unitless.}$$

5.5. Detector clicks

The detector clicks were counted with a Keysight 53220A frequency counter. The uncertainty on the mean was estimated from the counting statistics, after the subtraction of background counts

$$N_{\text{counts}} = 29744(46) \text{ s}^{-1}.$$

5.6. Dead time

The dead time of the detector was measured with a Fast Comtec MCS6A event time-tagger whilst the detector was illuminated by a flux corresponding to approximately 10k counts per second. An assessment of the time differences between adjacent detection events was used to evaluate both the dead time and recovery time (see figure 13 in [1]) of the device: the difference between these two response factors was found to be insignificant when applied to the DE calculation. A conservative uncertainty of 500 ps was assigned to τ_{d} , which was estimated by measuring the time-tagger's electronic jitter with regular electrical pulses provided by a Tektronics AWG70001A arbitrary waveform generator

$$\tau_{\text{d}} = 23.2(5) \text{ ns.}$$

6. Spatial response mapping

Spatial mapping of a detector's responsivity plays a crucial role in quantifying an uncertainty contribution which arises from non-uniformity; furthermore, non-uniformity can be a key parameter for applications where the spatial location of an incident source may vary as a function of time [41]. Mapping the response generally involves moving the detector relative to a fixed beam with translational staging whilst recording detector clicks as a function of excitation location [18]. However, within the FC-port of the Hamamatsu C13001-01 detectors sits a GRIN lens of unknown specification. As we are unable to remove the lens it is only possible to get an estimate of the detector's spatial uniformity. To do this, we placed detector SN1 into NPL's free-space detector calibration facility [23] and mapped the device's FC-port with a focused Gaussian beam with a 20 μm beam waist. The corresponding spatial response map, which is normalised by the maximum response value, is presented in figure 3.

To align the detector, we first optimised the position relative to the focal plane (z -axis): we defined optimal alignment to be the position at which the central 'uniform' area (see cross sections of figure 3) was maximised; as this area is greater than the footprint of the beam, it corresponds to the z -position at which the beam's waist was minimised. Once optimised, the detector's FC-port was mapped in the (x, y) plane. Centrally, within a diameter of approximately 30 μm , a uniform area is observed within which the relative standard deviation of DE values is 0.28%, with a maximum variation of $\pm 0.66\%$. Whilst this may only be taken as an approximation of the detector's non-uniformity, it suggests that the variation in DE values observed in the repeated coupling measurements are a result of incident light illuminating different areas of the sensor's surface when the fibre was re-coupled.

6.1. A comparison between fibre and free-space

The relatively flat central response of figure 3 is a strong indication that the active area can be under-filled with a carefully aligned free-space beam. This opens the possibility of measuring the DE of a fibre-coupled detector in a free-space configuration, enabling a direct comparison between fibre-coupled and free-space setups. To test this, we aligned the focused beam to the centre of the 'uniform' region (as marked by the circle within figure 3) and proceeded to measure SN1's DE in free space [23]; the measurements were then repeated on the same device in the fibre setup, as described in section 3. The comparison was performed with incident mean photon numbers ranging between 10^4 and 10^7 photons per second in both setups. Figure 4 displays the DE results which are corrected for dead time losses. The blue shaded area marks the spread of SN1's repeat coupling measurements at two standard deviations (see table 1). The red shaded area marks the free-space response variation within the central 30 μm of figure 3. The larger error bars present in the free-space data are due to a combination of uncertainty in the beam's location ($\pm 2.9 \mu\text{m}$) relative to

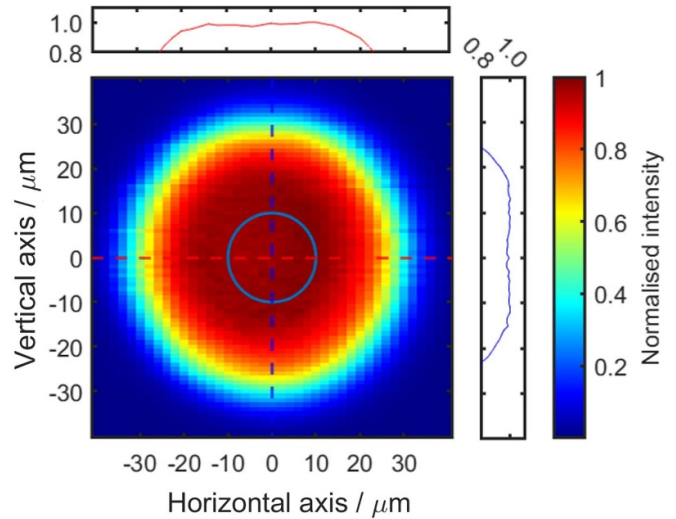


Figure 3. Spatial response scan of detector SN1's FC-port which houses a fixed lens. The red dashed line marks a horizontal (x -axis) cross section which is displayed above the figure; the blue dashed line marks the vertical equivalent which is displayed to the right of the figure; and the central circle indicates the beam's waist ($1/e^2$) at the focal plane.

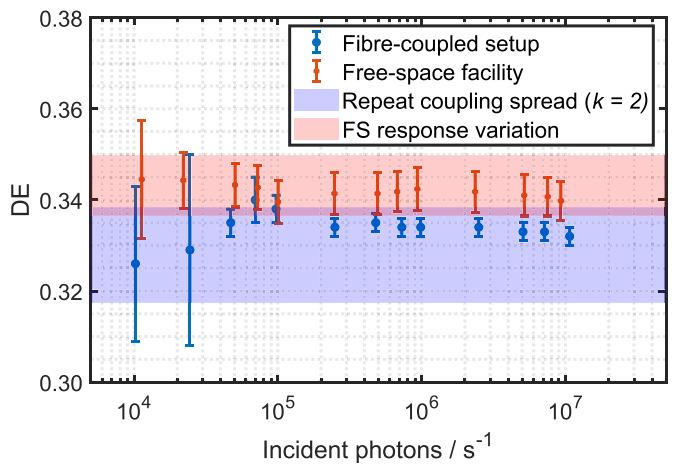


Figure 4. Detection efficiency plotted as a function of incident photon flux for a single detector (SN1), measured in the fibre-coupled setup and the free-space facility.

the DUT and the DUT's change in response within this uncertainty bound: in the fibre-based measurement the illumination area is assumed to be fixed, but unique to that specific coupling. The increase in measurement uncertainty at the lowest incident photon numbers, in both configurations, is a combination of the signal approaching the noise floor of their respective monitor photodiodes and counting uncertainty from the DUT.

The weighted mean DE values and standard uncertainties were calculated as before, using equations (5) and (6), with the i th measurement corresponding to a photon flux instead of a repeated coupling. Uncertainties were expanded to the 95%

confidence interval with coverage factors obtained from standard error propagation with the calculated effective degrees of freedom. The DE and expanded uncertainty was found to be 0.3336(12)% in the fibre setup and 0.3417(44)% in free-space. Although these results are not in agreement, they are only valid for their respective fibre-coupling/FS-alignment configurations. Both fall within two standard deviations of repeat coupling measurements (within uncertainty bounds) which is highlighted by the blue shaded region. However, a clear systematic shift between the two optical configurations is present, with only a small overlap between the two. At present, the cause of this is unclear and will be the focus of future work. There may be an effect caused by the two different optical modes incident upon the device in the two configurations. A more likely explanation is a systematic over-estimate of the number of incident photons in the fibre-based setup: photons reflected from the surface of PD_{ref} have the potential to scatter back onto the photodiode which would not be the case during its calibration. To reduce this effect, a black coating was applied to the internal surface of the photodiode's FC-port; however, a small fraction of photons may still be reflected. Finally, the assumption that the output of PD_{ref} and the SPADs are independent of polarisation at normal incidence may not be the case. In the next iteration we shall (1) employ SMF to couple to the DUT, (2) implement polarisation control and (3) consider using polarisation-maintaining fibre throughout. These changes will also make the setup suitable for the characterisation of superconducting nanowire single-photon detectors (SNSPDs).

7. Coupling repeatability

In this section, we assess the repeatability of fibre-to-fibre and fibre-to-detector couplings to identify the optimal coupling method. This was motivated by the inherent difficulty in accurately calibrating fibre-coupled single photon detectors [28], which is clear from the variations reported in section 4. We tested the repeatability of SMF couplings between standard FC/APC-to-FC/APC connectors via narrow key polarisation-maintaining (PM) interconnects and Diamond SA E2000-to-E2000 Simplex connectors (also APC) via their respective interconnects. All connectors were randomly selected. We also tested the repeatability of FC/PC-to-detector couplings to multiple SPADs with randomly selected SMF and MMF patch cables. A schematic of the setup is presented in figure 5 which consists of a fibre-coupled 633 nm CW source, a photodiode (PD_{mon}) to monitor common-mode noise, an optical MEMs switch which acts as a shutter, a VOA to provide attenuation, the two fibre connection types under test and a SPAD. Fibre specified for SM propagation at 633 nm was used throughout, except for the final fibre, which was alternated between SM600 and MMF depending on the measurement. The SPAD was placed in a light-tight enclosure to reduce background noise and the attenuation of the setup was set such that the SPAD was registering $\approx 10^5$ counts per second when illuminated.

Figure 6 displays the fibre-to-fibre repeat coupling results for the two connector types, with the y-axis representing the

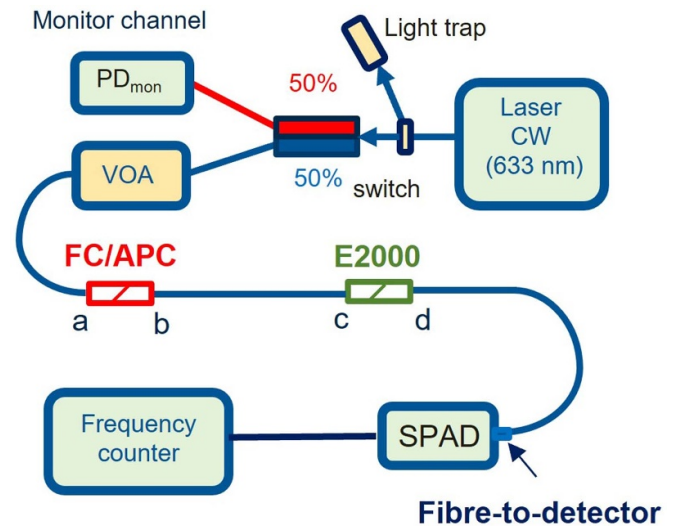


Figure 5. An illustration of the setup used to characterise the repeatability of E2000-to-E2000, FC/APC-to-FC/APC and FC/PC-to-detector couplings. A monitor photodiode (PD_{mon}) was used to monitor common-mode noise and an optical MEMs switch acted as the fibre shutter, enabling background subtractions. (a), (b) and (c), (d) mark the interconnect ports for the FC/APC and E2000 connectors, respectively.

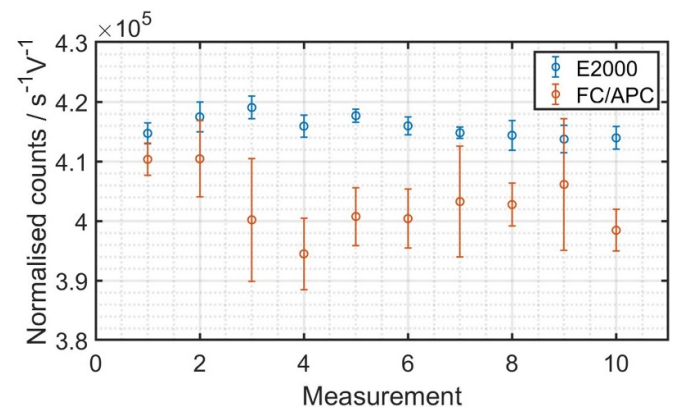


Figure 6. Repeat coupling results for E2000-to-E2000 and FC/APC-to-FC/APC connectors. The y-axis represents the mean number of detection events per second, normalised to the monitor photodiode output, after background subtractions. The x-axis gives the measurement set number. Error bars mark the standard deviation of the ten repeat couplings to a single port, forming a measurement set. Between each measurement set both fibres were disconnected and reconnected.

average count rate normalised by the monitor photodiode output, both of which were background subtracted. The E2000 connectors were tested first, error bars mark the standard deviation of ten coupling repeats to a single interconnect port (i.e. the port labelled (c) within figure 5). At the beginning of each measurement set, fibres were removed from both interconnect ports (i.e. (c) and (d)) which enables a comparison between re-coupling a single fibre and both fibres. After ten measurement sets the process was repeated with the FC/APC connectors.

Table 3. Coupling repeatability results for single-mode and multi-mode fibre couplings; standard deviations (Std. Dev) are evaluated with a coverage factor of $k = 1$.

| Detector | Single-mode Std. Dev | Multi-mode Std. Dev |
|------------------|----------------------|---------------------|
| Hamamatsu (SN5) | 0.85% | 0.15% |
| Laser Components | 0.88% | 0.68% |
| Excelitas (01) | 0.39% | 0.13% |
| Excelitas (02) | 0.55% | 0.22% |

For single port couplings the E2000 connectors are found to be the most repeatable, with a minimum (maximum) standard deviation of 0.23% (0.61%) across the ten measurement sets. Whereas the minimum (maximum) standard deviation for the FC/APC connectors was 0.66% (2.72%). These results are comparable with the standard deviation of repeat couplings to both ports which were 0.59% and 1.47% for the E2000 and FC/APC connections, respectively. The enhanced repeatability of the E2000 couplings is likely a result of the active crimping alignment mechanism which is employed to improve the precision and accuracy of core alignment [42]. There is also an element of user bias within these measurements; for example, the tightening of the FC/APC connector will vary from user-to-user, which ultimately affects the coupling efficiency. Given the care taken over these measurements, we assume these to be best case results.

The same setup was used to test the repeatability of directly coupling to a detector with the two fibre types. Four detectors from three manufacturers were tested: a single Laser Components COUNT-NIR, two Excelitas SPCM-AQRH detectors and an additional Hamamatsu C13001-01 (SN5). The two fibre types under test were a 1 m SM600 SMF with a 4.3 μm core diameter and a 1 m step-index MMF with a (10 ± 3) μm core diameter. Twenty repeat measurements were performed on each device with both fibre types, each containing a light and dark exposure enabling background subtractions. The attenuation between the monitor and SPADs was kept constant throughout, although it varied slightly when the final fibre was switched between SMF and MMF. All measurements were performed whilst each SPAD registered approximately 10^5 counts per second. The standard deviation of coupling repeats are summarised in table 3.

In all cases, the 10 μm core-diameter MMF was more repeatable than the 4.3 μm core-diameter SMF. We also note that the standard deviation of coupling repeats, as measured with the 50 μm core-diameter MMF within section 4 (refer to table 1), ranged between 0.69% and 1.60%. These results imply that the detectors are most uniform at distance scales comparable with the beam waist produced by the 10 μm core-diameter MMF. They also show that by employing 10 μm core-diameter MMF as the fibre which couples to the DUT, the repeatability can be significantly improve upon.

The variations observed in the fibre-to-detector couplings, as well as those measured with standard FC/APC connectors, make the E2000 connectors a viable option for improving repeatability. Moreover, with a specified insertion loss of

less than 0.1 dB, the use of E2000 connectors have the potential to be advantageous when minimising loss is critical. It is worth noting that although fusion-spliced fibre connections have been demonstrated to be highly effective [15], E2000 connectors offer a user-friendly alternative. They are also a practical option when the fibre cannot be easily removed from the DUT which allows the splicing loss to be characterised beforehand, as is the case with SNSPDs and many InGaAs SPADs. Finally, we note that in a recent measurement comparison between NMIs, E2000 connectors would have been beneficial as the FC/PC coupling repeatability to an InGaAs SPAD was, in one case, a dominant uncertainty [24].

8. Conclusion

A simple, portable setup which enables traceable optical power measurements in fibre at the few-photon level within the vis/NIR has been developed. The setup was used to characterise the DE of four Hamamatsu 13001-01 SPADs at a wavelength of 633 nm; moreover, the setup can be easily modified to accommodate other wavelengths as well as different detector types (e.g. SNSPDs). The weighted mean DE values of the four detectors had absolute standard uncertainties ranging between 0.20% and 0.27% ($k = 2$). These DE values, and corresponding uncertainties, give the best estimates of each detector's true efficiency; however, the standard deviations of coupling repeats must be considered as the act of re-coupling the fibre can vary the measured value significantly. This variation occurs due to changes in alignment between the fibre core, the lens and the sensor, where the sensor has an associated non-uniformity. To quantify the non-uniformity, one detector's spatially response was mapped through the GRIN lens housed in the FC-port of the detector. The estimated maximum variation in non-uniformity was found to be $\pm 0.66\%$ within the central 30 micron area, indicating that the repeatability of re-coupling a fibre is primarily due to the detector's non-uniformity. However, with this method only an estimate is possible due to mapping the sensor through a lens of unknown specification. In addition, a novel method for calibrating a fibre-coupled SPAD in a free-space configuration was presented. Since the free-space setup is well-established, we utilised this method as a preliminary validation approach. Finally, the repeatability of fibre-to-fibre and fibre-to-detector couplings were investigated. We found that the coupling between Diamond SA E2000 connectors were significantly more reproducible than standard FC/APC connectors. Furthermore, it was observed that the repeatability of the fibre-to-detector couplings were significantly better with the 10 μm MMF when compared with the 4.3 μm SMF and the 50 μm MMF.

Acknowledgments

This work was supported by Innovate UK Industrial Strategy Challenge Fund Projects 106178-45364 AIRQKD and 106374-49229 Assurance of Quantum Random Number

Generators (AQuRand), and the U.K. government department for Science, Innovation and Technology through the U.K. national quantum technologies programme. We also acknowledge David Szwer for his work on the data acquisition software and Stephen Giblin for his valuable insights during the review of this manuscript.

Appendix A. Attenuation linearity and stability

Figure A1 displays the six optical powers at which the attenuation ratio β was characterised. Eight data points are present, two of which were repeat measurements performed at the end. The inset, which is a closeup of the data within the central black rectangle, shows one of these repeat measurements.

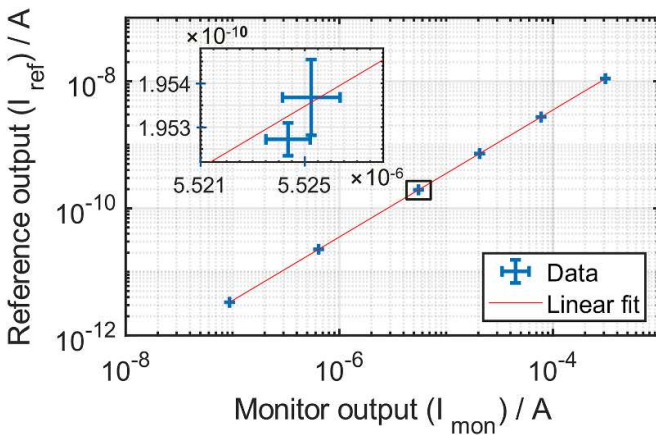


Figure A1. The reference photodiode's current output I_{ref} plotted as a function of the monitor photodiode's current output I_{mon} with a linear fit included.

As described in section 2, these eight points are constructed from five light and dark exposures each, totalling at forty background-subtracted data points taken over a 1.5 h period. The relative standard deviation of these forty points is approximately 0.1%.

Appendix B. Non-linear correction

The derivation of the DE equation for a CW source which considers the non-linearities that arise from dead time losses and the Poissonian nature of the source is described. Equations (B.1)–(B.4) are given for completeness, whilst the subsequent derivations follow the standard reasoning found in existing literature. Let n_m be the number of measured photons in a time interval T and n_d be the number of photons missed due to the detector's dead time (τ_d). The corrected number of incident photons (n_c) is then

$$n_c = n_m + n_d. \quad (\text{B.1})$$

Given a constant rate of incident photons, we may write

$$\frac{n_c}{T} = \frac{n_d}{n_m \tau_d}. \quad (\text{B.2})$$

Rearranging for n_d and substituting into equation (B.1) gives

$$n_c = n_m + \frac{n_c n_m \tau_d}{T}. \quad (\text{B.3})$$

Solving for the corrected number of photons yields

$$n_c = \frac{n_m}{1 - \frac{n_m \tau_d}{T}}. \quad (\text{B.4})$$

Next, the corrected probability of getting a click in the time interval δt for a Poissonian source may be expressed as follows

$$P(c|\delta t) = \frac{n_c \delta t}{T} = 1 - e^{-\eta \mu}, \quad (\text{B.5})$$

where μ is the mean incident photon number; i.e. $\mu = (N_{\text{inf}}) \cdot (\delta t)$. Substituting equation (B.4) into (B.5) gives

$$P(c|\delta t) = \frac{N_m \delta t}{(1 - N_m \tau_d)} = 1 - e^{-\eta \mu}, \quad (\text{B.6})$$

where N_m is the measured photon rate, i.e. $N_m = n_m/T$. Rearranging for η results in

$$\eta = -\frac{1}{\mu} \ln \left(1 - \frac{N_m \delta t}{1 - N_m \tau_d} \right). \quad (\text{B.7})$$

Finally, when $N_m \delta t (1 - \tau_d N_m)^{-1} \ll 1$, equation (B.7) may be written as

$$\eta \approx \frac{N_m \delta t}{\mu (1 - \tau_d N_m)} = \frac{N_m}{N_{\text{inf}} (1 - \tau_d N_m)}. \quad (\text{B.8})$$

ORCID iDs

Luke Arabskyj <https://orcid.org/0000-0002-2815-8032>
 Philip R Dolan <https://orcid.org/0000-0002-1071-7203>
 Ted S Santana <https://orcid.org/0000-0003-3610-9908>
 Simon R G Hall <https://orcid.org/0000-0002-5080-6008>
 Marco Lucamarini <https://orcid.org/0000-0002-7351-4622>
 Christopher J Chunnillall <https://orcid.org/0000-0002-5982-6865>

References

- [1] Chunnillall C J, Degiovanni I P, Kück S, Müller I and Sinclair A G 2014 Metrology of single-photon sources and detectors: a review *Opt. Eng.* **53** 081910
- [2] Villa F, Conca E, Madonini F and Zappa F 2021 SPAD 3D LiDAR sensors for automotive, industrial automation and surveillance *OSA Imaging and Applied Optics Congress 2021 (3D, COSI, DH, ISA, PcoAP)* (Optica Publishing Group) p CTh4E.1
- [3] Zickus V *et al* 2020 Fluorescence lifetime imaging with a megapixel SPAD camera and neural network lifetime estimation *Sci. Rep.* **10** 20986
- [4] Palubiak D, El-Desouki M M, Marinov O, Deen M J and Fang Q 2011 High-speed, single-photon avalanche-photodiode imager for biomedical applications *IEEE Sens. J.* **11** 2401–12

- [5] Barbieri C, Naletto G and Zampieri L 2023 Quantum astronomy at the university and INAF Astronomical Observatory of Padova, Italy *Astronomy* **2** 180–92
- [6] Wollman E E *et al* 2021 Recent advances in superconducting nanowire single-photon detector technology for exoplanet transit spectroscopy in the mid-infrared *J. Astron. Telesc. Instrum. Syst.* **7** 011004
- [7] Ma X, Yuan X, Cao Z, Qi B and Zhang Z 2016 Quantum random number generation *npj Quantum Inf.* **2** 1–9
- [8] Li W *et al* 2023 High-rate quantum key distribution exceeding 110 Mb s^{-1} *Nat. Photon.* **17** 416–21
- [9] Lucamarini M, Yuan Z L, Dynes J F and Shields A J 2018 Overcoming the rate–distance limit of quantum key distribution without quantum repeaters *Nature* **557** 400–3
- [10] Wengerowsky S, Joshi S K, Steinlechner F, Hübel H and Ursin R 2018 An entanglement-based wavelength-multiplexed quantum communication network *Nature* **564** 225–8
- [11] Yuan Z *et al* 2018 10-Mb/s quantum key distribution *J. Lightwave Technol.* **36** 3427–33
- [12] Dixon A R *et al* 2015 High speed prototype quantum key distribution system and long term field trial *Opt. Express* **23** 7583–92
- [13] Comandar L C, Fröhlich B, Lucamarini M, Patel K A, Sharpe A W, Dynes J F, Yuan Z L, Pentyl R V and Shields A J 2014 Room temperature single-photon detectors for high bit rate quantum key distribution *Appl. Phys. Lett.* **104** 021101
- [14] Lucamarini M, Patel K A, Dynes J F, Fröhlich B, Sharpe A W, Dixon A R, Yuan Z L, Pentyl R V and Shields A J 2013 Efficient decoy-state quantum key distribution with quantified security *Opt. Express* **21** 24550–65
- [15] Gerrits T, Migdall A, Bienfang J C, Lehman J, Nam S W, Splett J, Vayshenker I and Wang J 2020 Calibration of free-space and fiber-coupled single-photon detectors *Metrologia* **57** 015002
- [16] López M, Hofer H and Kück S 2015 Detection efficiency calibration of single-photon silicon avalanche photodiodes traceable using double attenuator technique *J. Mod. Opt.* **62** 1732–8
- [17] Jin J, Gerrits T and Gamouras A 2022 Calibration and comparison of detection efficiency for free-space single-photon avalanche diodes at 850 nm *Appl. Opt.* **61** 5244–9
- [18] Dhoska K, Hofer H, Rodiek B, López M, Kübarsepp T and Kück S 2016 Improvement of the detection efficiency calibration and homogeneity measurement of Si-SPAD detectors *SpringerPlus* **5** 1–14
- [19] Polyakov S V and Migdall A L 2007 High accuracy verification of a correlated-photon-based method for determining photon-counting detection efficiency *Opt. Express* **15** 1390–407
- [20] Bae I-H, Park S, Hong K-S, Park H S, Lee H J, Moon H S, Borbely J S and Lee D-H 2019 Detection efficiency measurement of single photon avalanche photodiodes by using a focused monochromatic beam tunable from 250 nm to 1000 nm *Metrologia* **56** 035003
- [21] Ghazi-Bellouati A, Razet A, Bastie J, Himbert M, Degiovanni I, Castelletto S and Rastello M L 2005 Radiometric reference for weak radiations: comparison of methods *Metrologia* **42** 271
- [22] Porrovecchio G, Šmid M, López M, Hofer H, Rodiek B and Kück S 2016 Comparison at the sub-100 fW optical power level of calibrating a single-photon detector using a high-sensitive, low-noise silicon photodiode and the double attenuator technique *Metrologia* **53** 1115
- [23] Chunnillall C J *et al* n.d. Traceable characterisation of free-space single-photon detectors in the visible/near-infrared (in preparation)
- [24] López M, Meda A, Porrovecchio G, Starkwood R, Genovese M, Brida G, Šmid M, Chunnillall C, Degiovanni I and Kück S 2020 A study to develop a robust method for measuring the detection efficiency of free-running InGaAs/InP single-photon detectors *EPJ Quantum Technol.* **7** 14
- [25] Chunnillall C, Lepert G, Allerton J, Hart C and Sinclair A 2014 Traceable metrology for characterizing quantum optical communication devices *Metrologia* **51** S258
- [26] Stephens M, White M G, Gerrits T, Tomlin N A and Lehman J H 2021 Quantum calibrations traceable through classical radiometry *Meas. Sens.* **18** 100267
- [27] Müller I, Klein R M and Werner L 2014 Traceable calibration of a fibre-coupled superconducting nano-wire single photon detector using characterized synchrotron radiation *Metrologia* **51** S329
- [28] Mueller I, Horansky R D, Lehman J H, Nam S, Vayshenker I, Werner L, Wuebbeler G and White M 2017 Verification of calibration methods for determining photon-counting detection efficiency using superconducting nano-wire single photon detectors *Opt. Express* **25** 21483–95
- [29] Bhargava A M, Rakshit R K, Das S and Singh M 2021 Metrology perspective of single-photon detectors: review on global calibration methods *Adv. Quantum Technol.* **4** 2100008
- [30] Avesani M *et al* 2021 Full daylight quantum-key-distribution at 1550 nm enabled by integrated silicon photonics *npj Quantum Inf.* **7** 93
- [31] Vedovato F *et al* 2023 Realization of intermodal fiber/free-space quantum key distribution networks *Proc. SPIE* **12446** 153–9
- [32] Martin J, Fox N and Key P 1985 A cryogenic radiometer for absolute radiometric measurements *Metrologia* **21** 147
- [33] 2023 Characterising the performance of free-space coupled single-photon detectors (available at: www.npl.co.uk/quantum-programme/capabilities/photon-detector)
- [34] Durak M, Samadov F and Türkoğlu A K 2002 Spatial non-uniformity measurements of large area silicon photodiodes *Turk. J. Phys.* **26** 375–80
- [35] Mountford J, Porrovecchio G, Smid M and Smid R 2008 Development of a switched integrator amplifier for high-accuracy optical measurements *Appl. Opt.* **47** 5821–8
- [36] Porrovecchio G, Smid M, Mountford J R, Cheung J Y, White M G and Chunnillall C J n.d. Sub pw traceable light radiation measurement technique with a photodiode and switched integrator amplifier (in preparation)
- [37] Durak M and Aslan M H 2004 Optical characterization of the silicon photodiodes for the establishment of national radiometric standards *Opt. Laser Technol.* **36** 223–7
- [38] Moision B, Srinivasan M and Hamkins J 2005 The blocking probability of Geiger-mode avalanche photo-diodes *Proc. SPIE* **5889** 137–46
- [39] Sciacca E *et al* 2003 Silicon planar technology for single-photon optical detectors *IEEE Trans. Electron Devices* **50** 918–25
- [40] JCGM 101:2008 2008 *Evaluation of Measurement Data—Guide to the Expression of Uncertainty in Measurement* (Joint Committee for Guides in Metrology)
- [41] Ursin R *et al* 2007 Entanglement-based quantum communication over 144 km *Nat. Phys.* **3** 481–6
- [42] Ferguson R, Hall S, Smith J, Pitwon R and Lee B 2022 Characterization of quantum grade interconnects *J. Phys.: Conf. Ser.* **2416** 012003